



This work was carried out in whole or in part within the framework of the NOMATEN Centre of Excellence, supported from the European Union Horizon 2020 research and innovation program (Grant Agreement No. 857470) and from the European Regional Development Fund via the Foundation for Polish Science International Research Agenda PLUS program (Grant No. MAB PLUS/2018/8), and the Ministry of Science and Higher Education's initiative "Support for the Activities of Centers of Excellence Established in Poland under the Horizon 2020 Program" (agreement no. MEiN/2023/DIR/3795).

The version of record of this article, first published in *Diamond and Related Materials*, Volume 147, August 2024, 111336, is available online at Publisher's website:
<https://dx.doi.org/10.1016/j.diamond.2024.111336>

This manuscript version is made available under the CC-BY-NC-ND 4.0 license.

CH₄ and CO₂ Adsorption Mechanisms on Monolayer Graphenylene and their Effects on Optical and Electronic Properties

A. Aligayev,^{1,2} F. J. Dominguez-Gutierrez,^{2,3} M. Chourashiya,^{2,4,5} S. Papanikolaou,² and Q. Huang⁶

¹Science Island Branch of Graduate School, University of Science and Technology of China, Hefei, 230026, China.

²NOMATEN Centre of Excellence, National Center for Nuclear Research, 05-400 Swierk/Otwock, Poland

³Institute for Advanced Computational Science Stony Brook University Stony Brook, NY 11749, USA

⁴Guangdong Technion Israel Institute of Technology, Shantou, 515063, China

⁵Technion, Israel Institute of Technology, Haifa, 32000, Israel

⁶University of Science and Technology of China, Hefei, 230026, China.

Graphenylene (GPNL) is a two-dimensional carbon allotrope with a hexagonal lattice structure containing periodic pores. The unique arrangement of GPNL offers potential applications in electronics, optoelectronics, energy storage, and gas separation. Specifically, its advantageous electronic and optical properties, make it a promising candidate for hydrogen production and advanced electronic devices. In this study, we employ a computational chemistry-based modeling approach to investigate the adsorption mechanisms of CH₄ and CO₂ on monolayer GPNL, with a specific focus on their effects on optical adsorption and electrical transport properties at room temperature. To simulate the adsorption dynamics as closely as possible to experimental conditions, we utilize the self-consistent charge tight-binding density functional theory (SCC-DFTB). Through semi-classical molecular dynamics (MD) simulations, we observe the formation of H₂ molecules from the dissociation of CH₄ and the formation of CO+O species from carbon dioxide molecules. This provides insights into the adsorption and dispersion mechanisms of CH₄ and CO₂ on GPNL. Furthermore, we explore the impact of molecular adsorption on optical absorption properties. Our results demonstrate that CH₄ and CH₂ affects drastically the optical adsorption of GPNL, while CO₂ does not significantly affect the optical properties of the two-dimensional material. To analyze electron transport, we employ the open-boundary non-equilibrium Green's function method. By studying the conductivity of GPNL and graphene under voltage bias up to 300 mV, we gain valuable insights into the electrical transport properties of GPNL under optical absorption conditions. The findings from our computational modeling approach might contribute to a deeper understanding of the potential applications of GPNL in hydrogen production and advanced electronic devices.

I. INTRODUCTION

Sensors detect gases through the physical adsorption of gas molecules onto a surface. These sensors use a gas-sensitive material, such as carbon-based ones, that change their properties upon gas adsorption, offering high sensitivity and selectivity¹. The high sensitivity of graphene to the local environment has shown to be highly advantageous in sensing applications, where ultralow concentrations of adsorbed molecules induce a significant response to the electronic properties of graphene²⁻⁷. Additionally, carbon-based materials can be tailored by varying their surface chemistry, porosity, and morphology. The hybridization of carbon atoms into sp⁻, sp²⁻, and sp³⁻ orbitals can create diverse carbon allotropes exhibiting distinct dimensionalities^{8,9}. Ongoing research focuses on improving the performance and reliability of gas adsorption sensors and exploring new materials and sensing mechanisms for enhanced gas sensing capabilities¹⁰⁻¹⁵.

Graphenylene (GPNL), an intriguing carbon allotrope sharing the same point group (D_{6h}) as graphene, is composed of sp²⁻ hybridized carbon atoms arranged in hexatomic and tetraatomic rings¹⁶⁻¹⁹. Qi-Shi Du et al. successfully synthesized layers of graphenylene, also referred to as biphenylene-carbon (BPC), by dehydrating and polymerizing 1,3,5-trihydroxybenzene^{20,21}. The process involved the removal of three water molecules from a 1,3,5-trihydroxybenzene molecule using dehydrant aluminum oxide, leading to the amalgamation of bare 6C rings (benzenes) and the formation of a small segment of the 2D

carbon crystal. Furthermore, polymerization could also take place through intermolecular dehydration between 1,3,5-trihydroxybenzene molecules, where the fragments of the 2D carbon crystal grew rapidly. The experimental construction of GPNL involved utilizing planar 4-carbon rings and 6-carbon rings with sp² electron configuration, experiencing slight distortions that ultimately resulted in the formation of a large planar conjugated π-system²². It possesses a hexagonal lattice structure with periodic pores, offering a high surface area and pore volume. These characteristics make GPNL a promising material for gas adsorption and separation applications. The unique topology of GPNL allows for selective adsorption of specific gas molecules, making it a potential candidate for highly efficient and selective gas separation and storage processes²³⁻²⁵. The identification of hollow adsorption sites in GPNL is of great interest, as these sites hold significant potential for various applications, including gas separation²⁶⁻²⁹.

The growing importance of air quality and safety has created a demand for advanced gas sensors. Porous carbon-based materials have emerged as promising candidates for such sensors due to their comparable electronic mobility and mechanical properties to graphene. Additionally, these materials offer the added advantage of enabling the dispersion of single atoms within acetylenic pores. Building upon the research progress in graphene, investigations into post-graphene 2D carbon-based materials have swiftly demonstrated diverse electronic devices and emerging charge transport phenomena. However, despite the growing understanding of electronic transport in individual 2D materials, practical wafer-

scale implementation faces significant challenges^{30,31}. Therefore, the development of reliable techniques for wafer-scale growth, ensuring uniformity and predictable thickness poses considerable hurdles from a materials science perspective. Thus, carbon materials exhibit versatile bonding abilities, ranging from sp^1 to sp^3 hybridization, and encompass a variety of allotropes, including fullerene, graphite, diamond, graphene, carbon nanotubes, and fibers³²⁻³⁴. Porous carbons can be obtained through the carbonization of natural or synthetic precursors, followed by activation, enabling tunability of pore sizes across a wide range, from micropores (< 2 nm) to mesopores (2-50 nm) and macropores (> 50 nm). Diverse synthesis strategies, such as template methods, etching of metal carbides, and sol-gel processing, have been explored to create porous carbon materials with controlled pore structures at both the micropore and mesopore levels³². These porous carbons find applications in crucial fields such as adsorption, separation, and electrode materials.

GPNL, with its exceptional porous architecture and remarkable electronic features hold great promise as a material for the development of high-performance molecular gas sensors. In order to save financial resources and avoid exhaustive experimental trials, detailed atomistic simulations are essential to complement practical exploration. In this study, we employ the Self-Consistent-Charge Density-Functional Tight-Binding (SCC-DFTB) method^{35,36} to investigate the potential applications of GPNL in the detection of important molecular gases such as CH_4 and CO_2 and their species, which have significant environmental implications^{37,38}. Here we investigate the hydrogen production through methane dissociation and CO_2 reduction mechanisms by emitting CH_4 , and CO_2 molecules with impact energies close to their dissociation energies and studying their interactions with GPNL. Additionally, we also compare our results with the findings obtained for graphene. Further computational research that closely emulates dynamic mechanisms observed in experiments is necessary to fully explore the potential of graphenylene, including its effects on optical absorption, electron transport performance, and enhancement of material sensitivity. Our primary objective is to contribute to the characterization of GPNL as a promising material for future research and the development of materials for ultrafast gas sensors and gas separation applications.

II. COMPUTATIONAL METHODS

The SCC-DFTB method is a computational approach that approximates traditional Density Functional Theory (DFT) by considering valence electron interactions in MD simulations. It serves as a valuable tool for accurately predicting structures and thermodynamic properties prior to synthesis, providing insights into the gas adsorption properties of 2D carbon-based materials and

their potential applications in various gas adsorption environments. The SCC-DFTB method involves solving Kohn-Sham equations to obtain total valence electronic densities and energies for each atom utilizing a Hamiltonian functional based on a two-center approximation and optimized pseudo-atomic orbitals as the basis functions^{35,36}. Slater-Koster parameter files are utilized to provide tabulated Hamiltonian matrix elements, overlap integrals, and repulsive splines fitted to DFT dissociation curves. These parameters describe the overlap and hopping integrals between pairs of atoms in the tight-binding Hamiltonian. The optimal set of Slater-Koster parameters have two main requirements: a good reproduction of the structure of the relevant electronic bands, and faithful representation of the orbital contribution along such bands. Therefore, in the scope of this approach the total energy of the system is expressed as

$$E^{\text{DFTB}} = E_{\text{band}} + E_{\text{rep}} + E_{\text{SCC}}, \quad (1)$$

with the band structure energy, E_{band} , defined from the summation of the orbital energies ϵ_i over all occupied orbitals Ψ_i ; the repulsive energy E_{rep} for the core-core interactions related to the exchange-correlation energy and other contributions in the form of a set of distance-dependent pairwise terms; and an SCC contribution, E_{SCC} , as the contributions given by charge-charge interactions in the system. Therefore, the electronic energy is calculated by summing the occupied Kohn-Sham (KS) single-particle energies and the contributions from repulsive energies between diatomic atoms. To account for self-consistent charge (SCC) effects during the dynamics, an iterative procedure is used.

A. Structures and binding energies

GPNL is a two-dimensional carbon allotrope that possesses a hexagonal lattice structure with periodic pores and its structure as reported by Balaban et al.¹⁶ and Martins et al.²⁴, consists of three types of symmetrically distributed rings: dodecagon (C_{12}), hexagon (C_6), and square (C_4), which forms a tiling of the Euclidean plane. The unit cell of GPNL, determined by Fabris et al. using DFT³⁹, belongs to the $P6/mmm$ space group and contains a single irreducible atom, which is considered in our SCC-DFTB calculations. In our study, we performed optimization of the GPNL unit cell, resulting in lattice parameters $\vec{a} = \vec{b} = 6.735$ Å and bond lengths of 1.50 Å for the square ring and 1.48 Å for the hexagon ring identifying seven points of high symmetry⁴⁰ which is in good agreement with experimental measurements for 1.42-1.46 Å for the 6-C rings and 1.50-1.52 Å for the two bonds joining the 6-C rings²⁰, as shown in Fig. 1a). The central nanopore (dodecagon ring) in the unit cell has a diameter of 5.66 Å, in good agreement with DFT data^{18,39} and experimental measure of 5.8 Å²⁰. To compare the adsorption capabilities of GPNL with graphene,

we also optimized the unit cell of graphene using a well-known lattice parameters and bond lengths, as depicted in Fig. 1b).

The interaction potentials between H_2 , CO_2 , and CH_4 molecules with graphene and GPNL are investigated using the DFTB method. To avoid interactions with periodic replicas, the unit cell of the optimized GPNL structure is replicated by $3 \times 4 \times 1$ and the unit cell of graphene is replicated by $5 \times 5 \times 1$ along the x and y directions. The larger cells are initially optimized using SCC-DFTB. Adiabatic calculations follow to determine potential energy curves. These curves depict molecule interactions with fully relaxed periodic sheets at different distances and adsorbate sites, incorporating dispersion corrections through van der Waals interactions.⁴¹ Thus, the total energies, $E(z)$, of the molecule–2D material system with a separation z between the adsorbate sites and the center of mass of the molecules are varied above the surface in a range of 0.5 to 7 Å, which defines the computation of the adsorption potential as a function of the distance separation. The total energy is then computed as:

$$E(z) = E_{\text{Tot}} - (E_{2\text{Dmaterial}} + E_{\text{Molecule}}), \quad (2)$$

where E_{Surface} is the total energy of the 2D material; E_{Molecule} is the total energy of the isolated molecule: H_2 , CH_4 , and CO_2 ; and E_{Tot} is the energy of the interacting system at every z -distance. Thus, the binding energy is defined as $E_b = E(z_{\text{min}})$ with z_{min} as the equilibrium

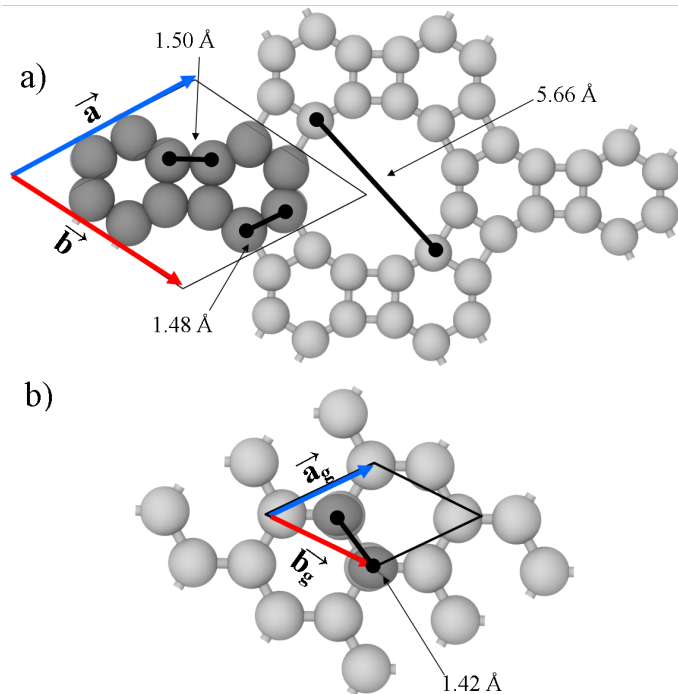


FIG. 1. (Color online). Optimized structures of graphenylene (a) and graphene (b) were obtained using the SCC-DFTB method. The calculated bond lengths and lattice parameters are in good agreement with the reported DFT data³⁹.

molecule–surface distance. Total energy calculations are performed for the molecule–2D material system, varying the distance between the surface and the center of mass of the molecules along the z -axis. We consider 3 different adsorption sites for graphene and 5 sites for GPNL based on unit cells of the materials. The molecular symmetry planes are considered with respect to the surface plane in the calculations. The repulsive potential is cut off at a distance below the second nearest-neighbor interaction region for numerical stability.

B. Semi-Classical Molecular Dynamics Simulations

We conducted semi-classical molecular dynamics simulations to investigate the adsorption dynamics of H_2 , CH_4 , and CO_2 molecules on graphene and GPNL. For graphene, a $5 \times 5 \times 1$ supercell was used, while for GPNL, a $3 \times 3 \times 1$ supercell was employed. The surfaces were optimized and equilibrated to a temperature of 300 K using a Nose–Hoover thermostat. To simulate the adsorption dynamics, we defined a target area of 1 nm² on the surface, and molecules were randomly distributed on it using the velocity Verlet algorithm. The impact energy of the molecules was 8 eV, and 650 independent trajectories were generated for each molecule. A time step of 0.25 fs was used, and the molecules were emitted vertically with random orientations at an initial distance of 0.6 nm above the surface. The simulations were performed for a duration of 350 fs. This timeframe was meticulously chosen to ensure convergence in our MD simulations. It provided ample time for the molecules to travel away from the carbon sheets while also guaranteeing that the attached molecules remained bonded to the carbon atoms, preventing any detachment from the sheets. We have previously employed this approach to study hydrogenation mechanisms of fullerene cages⁴², electronic properties of borophene⁴³, and dynamic physisorption pathways of molecules on alumina surfaces⁴⁴, demonstrating excellent agreement with first principles DFT calculations.

C. Optical absorbance and electron transport calculations

The optical absorption is investigated within the DFTB framework as an electronic dynamic process in response to an external electric field^{45,46}. The conventional adiabatic approximation gives the time evolution of the electron density matrix by time integration of the Liouville–von Neumann equation expressed as

$$i\hbar \frac{\partial \hat{\rho}}{\partial t} = S^{-1} \hat{H} \hat{\rho} - \hat{\rho} S^{-1}, \quad (3)$$

where $\hat{\rho}$ is the single electron density matrix, \hat{S} is the overlap matrix, and \hat{H} is the system Hamiltonian that includes the external electric field as $\hat{H} = \hat{H}_0 + E_0 \delta(t -$

$t_0)\hat{e}$ with E_0 , the magnitude of the electric field, and \hat{e} , its direction. Under the framework of linear response, the absorbance $I(\omega)$ is calculated as the imaginary part of the Fourier transform of the induced dipole moment caused by an external field. In this study, the external field strength was set to $E_0 = 0.001 \text{ V/\AA}$. The induced dipole moment was evaluated over a 200 fs time period using a time step of $\Delta t = 0.01 \text{ fs}$. The Fourier transform was performed with an exponential damping function (using a 5 fs damping constant) to eliminate noise.

The Non-Equilibrium Green's Functions formalism (NEGF) is a robust theoretical framework commonly used for modeling electron transport in nano-scale devices and is implemented in the DFTB code⁴⁷. In Fig. 2, we provide a detailed illustration of the geometric configuration of the graphene and GPNL structures, highlighting the specific regions involved in the electron transport calculations. To ensure accurate and reliable results, several steps are followed: 1) The structures are carefully divided into distinct sections, including the principal layers, two electrode contacts (drain and source), and the device region. This partitioning enables a systematic analysis of electron transport within the designated "scattering region."; 2) The drain section, represented by red spheres, corresponds to the region where electrons exit the device, while the source section, depicted by blue spheres, represents the region where electrons enter the device; 3) To simulate realistic conditions and investigate the impact of specific molecules on electron transport, CO_2 molecules are introduced into the graphene device section, and CH_4 molecules are added to the GPNL device section. This allows us to study the interaction between the adsorbates and the carbon-based materials and observe their influence on the electron transport properties; and 4) Before performing the electron transport calculations, the entire system undergoes an optimization process. This optimization involves adjusting the positions and orientations of the atoms to find the most energetically favorable configuration for the combined graphene/GPNL-adsorbate system.

III. RESULTS

GPNL exhibits lower electric conductivity compared to graphene due to its distinct physical properties, particularly its formation energies and band gaps. The influence of pore size and quantity on these properties is depicted in Fig. 3. Our DFTB calculations reveal that GPNL possesses a bandgap of approximately 0.96 eV from the DOS calculations, while graphene lacks a bandgap altogether. The porosity of GPNL has the potential to significantly modify its electronic characteristics and catalytic performance by increasing its surface area, in good agreement with reported results by G. Brunetto et al²². The electronic band structures, illustrated in Fig. 3, reveal that the valence and conductance bands for carbon atoms are located at the Γ point. The band gap of GPNL

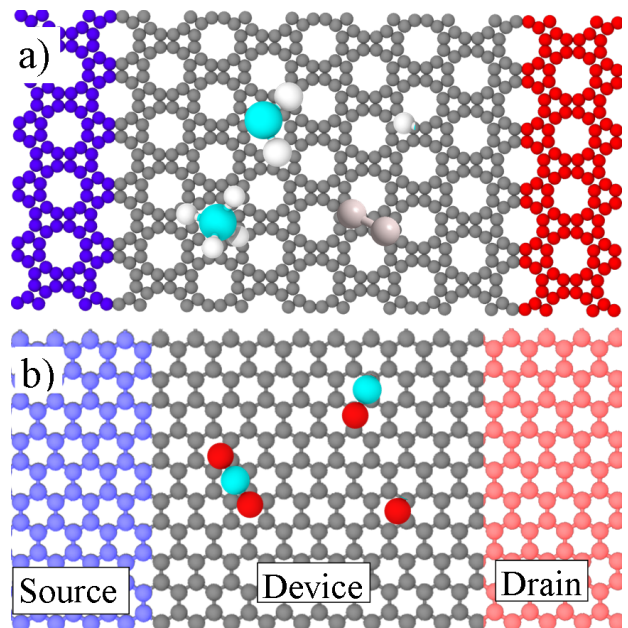


FIG. 2. Optimized structures employed in the electron transport calculations. In (a), the structure is shown for graphenylene with CH_4 , CH_2 , and H_2 molecules and a hydrogen atom attached, while in (b), graphene sheet is depicted with CO_2 and CO molecules with an oxygen atom. The blue and red regions represent the two principal layers. The middle region corresponds to the device under investigation and the size of the molecules is increased for better visualization.

is structure-dependent and can range from zero to a few electron volts. Theoretical studies have predicted band gaps for GPNL ranging from 0 eV to approximately 3.3 eV, depending on the specific structure and calculation method employed^{2,22}. It should be noted that the semi-local functionals tend to underestimate the band gaps of GPNL structures. It is also noticed the selected path show the characteristic gaps at the M and Γ point reported by DFT calculations¹⁸ and our results reported in the SM. The slight discrepancy in negative energies can be attributed to variations in the SK parameters applied in our calculations and the pseudo potentials used in our DFT calculations. Nevertheless, this fair agreement still provides validation for our results.

To validate our findings, density functional theory (DFT) calculations were conducted using the PBE exchange-correlation functional. The calculations were carried out under periodic boundary conditions, and the Brillouin zone integration was performed with the Γ point considered. Kohn-Sham orbitals were employed as plane waves up to an energy cutoff of 90 Ry to ensure convergence in the structural properties of the systems. The Quantum-ESPRESSO ab-initio package with relativistic-corrected pseudo-potentials was utilized for computing the density of states, system energies, and band structures. The total electronic density of states (DOS) for GPNL reveals significant overlaps between the C-2s and C-2p curves, indicating the presence of strong

sp^3 hybridized covalent bonding states.

GPNL consists of interconnected benzene rings arranged in a hexagonal lattice, similar to graphene. The slight discrepancy in negative energies for the GPNL sheet can be attributed to variations in the SK parameters applied in our calculations and the pseudo potentials used in our DFT calculations. Nevertheless, this fair agreement still provides validation for our results. This supports the application of SCC-DFTB in studying gas separation processes, which is crucial for the production and utilization of clean fuels. Different paths for the GPNL sheet was considered and shown in the supplementary material (SM) of this work.

Figure 4 illustrates the binding energies as a function of separation distance for graphene (a) and GPNL (b), considering different adsorbate sites as labeled in the inset figure. We performed adsorption calculations for isolated H_2 , CH_4 , and CO_2 molecules on both systems. To en-

sure accurate calculations, we included a 50 Å vacuum section above the sample to minimize boundary effects. Periodic boundary conditions were applied in the x - y directions to simulate a semi-infinite surface. For the k -point sampling, we employed a $4 \times 4 \times 1$ Monkhorst-Pack set throughout all calculations.

Fig. 4 present results for the physisorption pathways for H_2 , CH_4 , and CO_2 molecules on both graphene and GPNL sheets. In the case of graphene, we observe that the bond length for molecular hydrogen and methane molecules is approximately 2.2 Å, with binding energies of -0.052 eV (in good agreement with Lee et al.⁴⁸) and -0.165 eV, respectively. Meanwhile, the carbon dioxide molecule exhibits a bond length of 2.6 Å and a binding energy of -0.151 eV. For GPNL, we find that H_2 and CH_4 molecules have bond lengths of 2.25 Å, with binding energies of -0.043 eV and -0.132 eV, respectively. CO_2 on GPNL has a bond length of 2.62 Å, accompanied by a binding energy of -0.125 eV. In the SM, we present the physisorption pathways of all the adsor-

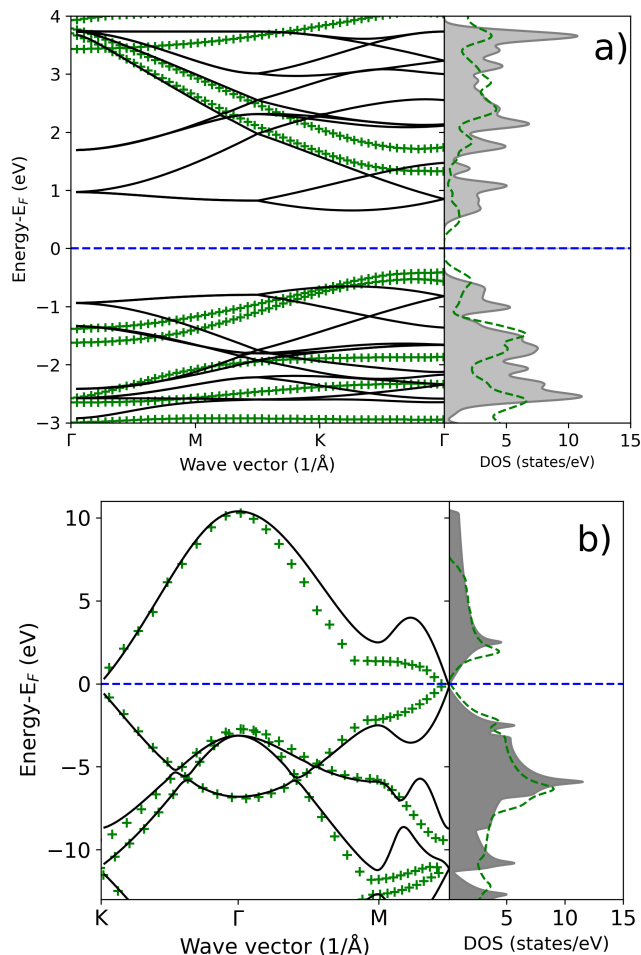


FIG. 3. Band structure and density of states for GPNL in a) and for graphene in b). Similarities are observed due to the hexagonal arrangement in the unit cell of the materials. DFT calculations are represented by dashed lines for the density of states (DOS) and marked with cross-points for the band structure.

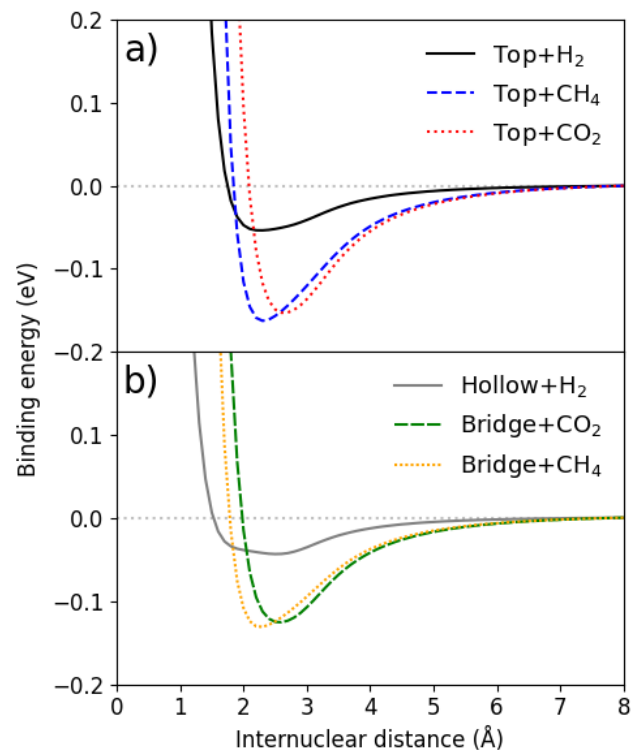


FIG. 4. Binding energies are presented as a function of separation distance for both graphene (a) and graphenylene (b), showcasing the lowest energy states and the impact of distinct adsorbate sites on the binding of H_2 , CO_2 , and CH_4 molecules. The analysis reveals a stronger tendency for adsorbate molecules to form bonds with the top carbon atoms in graphene, while graphenylene displays diverse adsorbate sites due to its sp hybridization. The remaining potential energy curves (PECs) can be found in the Supplementary Material accompanying this manuscript.

bate site of both carbon sheets, showing that adsorbate sites associated with the hexagonal and square holes exhibit a lower likelihood for molecule adsorption; specially methane molecules are more likely to bond to the top of the carbon atoms, with a binding energy of -0.2 ± 0.05 eV showing excellent conditions for gas separation for this energy barrier^{18,25}.

These results serve as the basis for configuring the initial conditions in our MD simulations. We ensure an initial distance greater than 8 Å to prevent interactions between the molecules and the carbon sheet at the outset of the simulation. These findings offer valuable insights into the interactions between carbon sheets and these molecules, which are essential for understanding the physical processes in our MD simulations. It is worth noting that dispersion corrections play a significant role in these calculations, particularly due to the hybridization of the system and the presence of CH₄ molecules. Similar trends are observed for graphene, where the adsorbate site located at the top of the carbon atoms is more favorable for both physisorption and chemisorption mechanisms confirming reported results for hydrogen trapping by graphene⁴¹, indicating a higher likelihood of attracting molecules.

A. Dynamical adsorption of CH₄ and CO₂ molecules

After conducting MD simulations at room temperature and an impact energy of 8 eV, the emission of hundreds of H₂, CO₂, and CH₄ molecules is analyzed by calculating the probabilities of adsorption, reflection, and transmission, which are defined as:

$$P = 100 \times \frac{N_x}{N_{\text{Tot}}}, \quad (4)$$

where N_{Tot} is the total number of MD simulations, while N_x is the number of cases for adsorption, reflection, and transmission calculated by using the following conditions based on the last frame of the MD simulations: 1) Adsorbed cases: Molecules with a final position between a sphere centered at the material with a radius of 3.5 Å and the direction of the velocity vector points towards the surface is considered as adsorbed; 2) Reflection cases: Molecules with a final position larger than 3.5 Å and a velocity vector oriented in the opposite direction to the surface normal is counted as reflected; 3) Transmission cases: Molecules with a final position below the surface and a distance larger than -3.5 Å are counted as transmitted. The counts for these cases are tabulated in Table I.

For graphene, we did not observe dissociation of H₂ and CO₂ molecules among the reflected molecules. The molecule initiates its trajectory with a kinetic energy (KE) of 8eV. However, it undergoes a gradual deceleration as it comes into contact with the charge cloud of the carbon sheets. Upon colliding with a carbon sheet at

| | Graphene | | | Graphelyne | | |
|--------------|----------------|-----------------|-----------------|----------------|-----------------|-----------------|
| Probability | H ₂ | CO ₂ | CH ₄ | H ₂ | CO ₂ | CH ₄ |
| Transmission | 0 | 0 | 0 | 5.28 | 1.28 | 49.12 |
| Adsorption | 0 | 0 | 16.8 | 0 | 9.66 | 1.60 |
| Reflection | 100 | 100 | 83.2 | 94.72 | 89.06 | 49.28 |

TABLE I. probabilities of different cases observed in the MD simulations, including transmission, reflection, and adsorption, for both graphene and GPNL. The results clearly demonstrate that GPNL exhibits superior performance as a material for gas separation compared to graphene.

various adsorbate sites, the molecule is reflected, promoting its vibrational and rotational movements. To observe dissociation mechanism, a higher impact energy than 10 eV would be required. However, it is worth noting that such high-energy collisions could result in the creation of vacancies in the graphene sheet by displacing a carbon atom, which is not observed in our MD simulations at 8 eV. On the other hand, some of the reflected CH₄ molecules underwent dissociation, and a few of them were able to attach to the graphene sheet. In order to bond more CH₂ molecules to graphene, a lower impact energy would be sufficient. In the case of GPNL, its inherent porosity allowed for a higher number of transmitted cases for both H₂ and CO₂ molecules. We observed that some carbon dioxide molecules dissociated into CO+O, with the CO molecules bonding to the GPNL sheet. This highlights the advantage of GPNL's porous structure in facilitating gas transmission and reactivity compared to graphene.

From our MD simulation results, we have observed that CH₄ molecules can undergo reflection and dissociation, leading to the formation of CH₂ and H₂ as the main process. Figure 5 displays a histogram of the counts of the final positions of the C and H atoms for the final frames of the simulations for graphene (a) and GPNL (b), providing a visual representation of the observed dynamics. This plot is used to count for the number of events with a probability of transmission, reflection, or absorption. In the figures, we correlated the visualization all the events to the histogram by shown the last frame of all the MD simulations in a single image where C atoms forming graphene and GPNL are represented as gray spheres, adsorbed CH₂ molecules are depicted as black spheres for C atoms and white spheres for hydrogen atoms, while reflected molecules are represented by turquoise spheres for molecular hydrogen and purple spheres for C atoms. Within our observations, we find that CH₂ molecules are more likely to binding to the carbon sheets. In alternative scenarios, both CH₂ and H₂ molecules are seen to dissociate after collision with the carbon sheets. A notable observation is the differential behavior of hydrogen molecules in graphene compared to GPNL.

The GPNL's porous structure facilitates the trans-

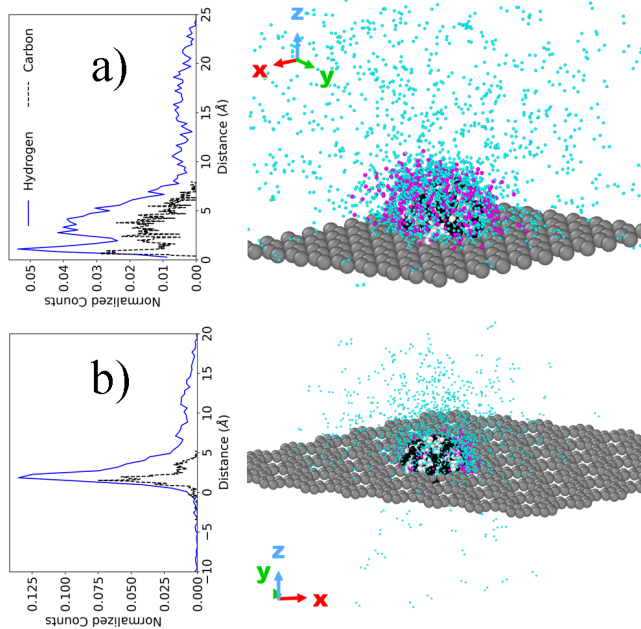


FIG. 5. The visualization of the final frame in each MD simulation simultaneously enables a thorough analysis of the adsorbed, reflected, and transmitted cases for both Graphene (a) and graphenelyne (b); with their corresponding histogram for the distance counts on the z-axis. The structures consist of carbon atoms depicted as gray spheres. Adsorbed CH_2 molecules are represented by black spheres for carbon atoms and white spheres for hydrogen atoms. Reflected molecules are shown as turquoise spheres representing molecular hydrogen, and purple spheres representing carbon atoms.

mission of hydrogen molecules, making it a promising candidate for applications such as hydrogen production in the context of energy generation. While graphene sheets present high scattering of H_2 molecules. We have found that CH_4 molecules are unable to transmit through graphene, whereas in the case of GPNL, there is a probability of approximately 50% for transmission, accompanied by dissociation and the production of molecular hydrogen. This behavior can be attributed to the porous nature of the materials and the impact energy of the emitted. In addition, we analyze the velocity distributions of carbon (C), oxygen (O), and hydrogen (H) atoms at the last frame considering all the MD simulations for each case. Notably, molecular hydrogen exhibits the highest velocities, while CH_2 molecules exhibit the lowest velocities after being reflected by the carbon sheets. This observation provides an initial indication of the bonding behavior of the ejected molecules, which is discussed in more detail within the SM.

Furthermore, we have noted that CH_2 molecules can form bonds with GPNL by infiltrating the porous structure and binding to the underlying C atoms. This property distinguishes GPNL from graphene, as the latter typically requires the presence of defects to enable

molecule transmission. Here, the distinctive arrangement of sp^2 -carbon atoms in GPNL creates a two-dimensional lattice with regularly spaced sized pores which is notably larger than the kinetic diameters of H_2 , CO_2 , and CH_4 , facilitating the favorable diffusion of these molecules. This mechanism highlights the potential of GPNL is a promising material for gas separation, particularly for CH_4 , as supported by our MD simulations for CO_2 purification as well.

Figure 6 presents the analysis of reflected molecules from the surfaces of graphene and GPNL at an impact energy of 8 eV. The analysis involves determining the internuclear distance between atoms in the final frame of the simulations. In the case of H_2 molecules (Figure 6a), we observe a uniform distribution of the internuclear distance around the bond length of 0.74 Å. This distribution arises from the excitation of vibrational and rotational states due to the exchange of kinetic energy during a collision with the surfaces, as previously discussed. For CO_2 molecules, we observe the splitting of the molecules into CO and O, with a majority exhibiting a homogeneous distribution around 1.43 Å for the internuclear distance which corresponds to the CO bond length. Oxygen atoms are identified with an internuclear distance larger than 2.5 Å. Finally, CH_4 molecules undergo splitting into CH_2 and H_2 molecules with the highest probabilities, with CH_3+H dissociation with a low probability. Molecular hydrogen is characterized by an internuclear distance of around 0.74 Å and a higher degree of excitation in vibrational states. We identify CH_2 (methylene) molecules as the main dissociation channel with a peak in the histogram at 1.8 Å being the internuclear distance between H atoms. The porosity of GPNL makes it a more promising candidate for H_2 production compared to graphene, as demonstrated by MD simulations. The histogram illustrates the distribution of reflected molecules with different bond lengths corresponding to their excited vibrational states. For instance, when H_2 molecules are emitted onto the 2D materials, they tend to vibrate towards states close to their ground state. On the other hand, H_2 molecules originating from the dissociated methane exhibit various bond lengths due to their excited vibrational and rotational states. This concept also applies to CO_x and CH_x molecules.

B. Optical Absorption Spectra, electron transport and sensitivity

Before performing the optical absorption calculations, We conducted unconstrained optimizations of the carbon sheet in the presence of various molecules and atoms, each in different scenarios. In instances where a physisorption pathway was relevant, constrained optimization calculations were performed to establish the optimal bond lengths. This approach was adopted to simplify the computational process, allowing for a more efficient and accurate determination of the atomic configurations.

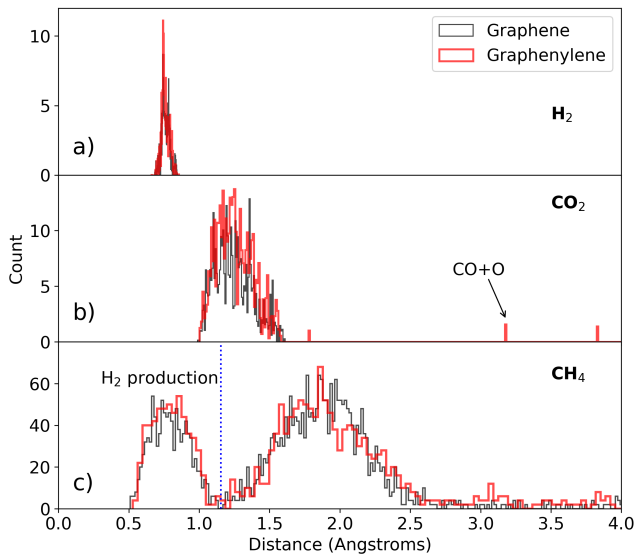


FIG. 6. Analysis of reflected molecules from graphene and graphenylene surfaces. Upon collision, H_2 molecules are reflected without breaking their bonds, but changing their angular momentum. Most of the CO_2 molecules are reflected, while a fraction of them undergo dissociation into CO and O. Interestingly, the collision with the surfaces results in the production of H_2 for the majority of CH_4 molecules.

The optical spectra are calculated for different cases of molecular adsorption: 1) For hydrogen molecules, we considered a single H_2 molecule positioned above a carbon atom, as well as two hydrogen atoms positioned above two different carbon atoms, where the interaction between them is minimal; the obtained results are in a good agreement with experimental and ab-initio data where the absorption intensities of the interband transitions occurring in the Dirac band (mid-IR and visible)^{34,49,50}. 2) For CO_2 and its split $\text{CO}+\text{O}$ molecule, we positioned the CO_2 molecule above a carbon atom, and for the resulting $\text{CO}+\text{O}$ system, we placed it above two different carbon atoms. The effect of carbon dioxide on the graphene sheet is similar to that observed for the H_2 molecule. For GPNL, the influence decreases compared to the pristine case. However, the split of $\text{CO}+\text{O}$ enhances the absorbance of the graphene sheet at the same wavelength as the CO_2 molecule. For the GPNL case, the absorbance rate is lower than that observed in the carbon dioxide case. 3) For methane molecules, we investigated several configurations: CH_4 , CH_2+H_2 (molecular hydrogen and methylene as a main dissociation channel), $\text{CH}_2+\text{H}+\text{H}$, and CH_2 , as they are crucial for sensor development^{27,51}.

Figure 7 presents the normalized optical absorption spectrum of graphene (a) and GPNL (b) obtained using the Liouville–von Neumann equation for the hydrogen molecule, methane, and carbon dioxide and the rest of the results are displayed in the SM. These findings reveal that pristine graphene doesn't interact with visible

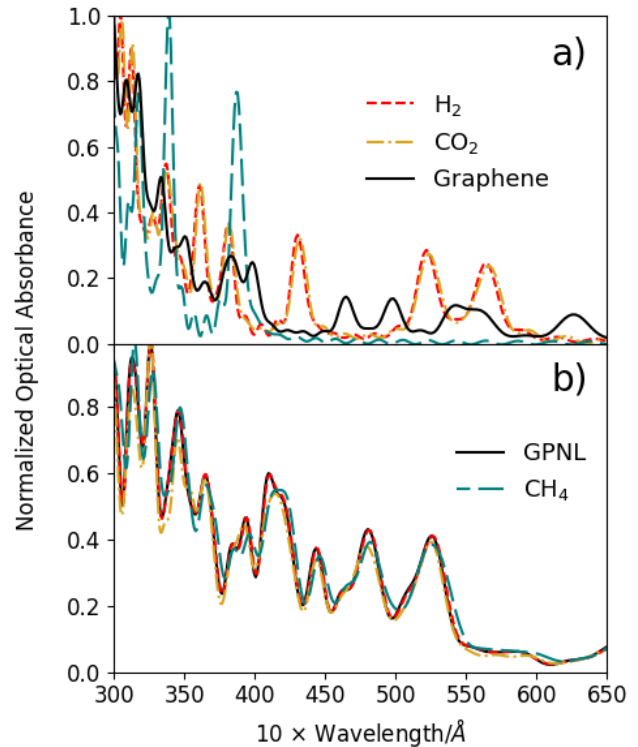


FIG. 7. Optical absorbance spectra of graphene (a) and graphenylene (b) in the visible range, considering H_2 , CO_2 , and CH_4 molecules adsorbed by the surfaces. The presence of split CH_4 molecules significantly impacts both surfaces.

light, as expected⁵². However, when it's paired with a hydrogen molecule or carbon dioxide, graphene becomes more effective at absorbing visible light. In contrast, the addition of a methane molecule primarily enhances its ultraviolet absorption capabilities. Furthermore, when it comes to the GPNL, the presence of attached molecules doesn't exert any discernible effect on the optical properties of the carbon sheet. The structural characteristics of the pores do not significantly enhance light absorption, and its band gap doesn't cause excessive scattering of visible light. This underscores the material's stability in maintaining its optical properties across diverse conditions. In the SM, we noticed that among all the configurations, the optical absorbance is maximized in the 300–450 wavelength range for the $\text{CH}_2+\text{H}+\text{H}$ case, attributed to the bonding between H atoms and the C atom of graphene. In contrast, in the case of GPNL, CH_2 increases the optical absorbance in the range of 400 to 550 wavelengths due to the system's hybridization and modifying the DOS.

Advancements in 2D materials have expanded the scope of potential applications, particularly in energy harvesting and storage, due to their high electron transport efficiency and extensive surface area with numerous active sites⁵³. In our study, we adopted a computational approach based on a π -orbital tight-binding Hamil-

tonian to simulate the electrical transport phenomena of graphene and GPNL. We employed the SCC-DFTB method along with Non-equilibrium Green's functions⁴⁷. In the tight-binding representation, the interaction between atoms is limited to a finite range. We can solve the contact self-energy function, also known as the surface Green's function, for the matrix block corresponding to the atoms near the extended device region using a recursive algorithm¹⁹. This allows us to accurately describe the electrical transport properties of the materials and analyze their behavior under various conditions.

Figure 8 illustrates our findings for graphene in a) and GPNL in b) that are in good agreement with reported results for pristine graphene in the literature and by Villegas et al.¹⁹ for the pristine GPNL; by adding different molecules it is revealed the preferential adsorption of extrinsic chemical species like CH₄, CO₂, and H₂ at interdomain sites, leading to a significant enhancement of scattering effects in both graphene and GPNL. To delve into this intriguing behavior, we employed the non-pulsating direct current (NPDC) waveform, known for its ability to maintain the stability of adsorbates even under ultrahigh-vacuum conditions. Unlike PDC waves, which exhibit continuous voltage fluctuations, NPDC

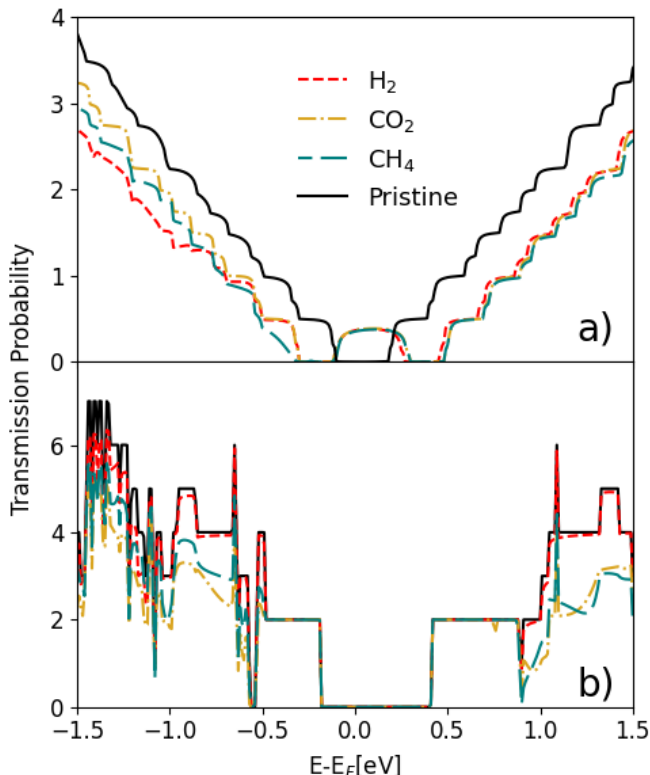


FIG. 8. The total transmission probabilities summed over all channels in the nanoribbon graphene direction in a) and through the pores of graphenelyne in b) for the pristine surface and with different molecules observed during the bombardment simulations.

waves maintain a constant voltage, ensuring the stability of the adsorbed species within the scope of our computational approach. For graphene, it is noteworthy that the adsorption of individual hydrogen, carbon dioxide, and methane molecules leads to a reduction in the transmission probability. This reduction has a direct impact on the density of states within the altered system. Additionally, it is observed that the effects on the DOS of the armchair-wise graphene sheet is associated with the bond formed between carbon atoms and these molecules; which are reflected in the transmission probability of two symmetric minima around the Fermi. On the other hand, when considering the GPNL sheet, the presence of singly bonded molecules to carbon atoms does not appear to induce substantial modifications in the transmission probability. However, there is a decrease in the transmission probability within the energy range of approximately ± 1.5 to 1.0 eV. This observation highlights the potential of GPNL as a promising candidate for the development of gas sensors, emphasizing its sensitivity to changes in its surrounding gaseous environment. Since, the strong mechanical properties play a key role in maintaining the structural integrity of porous frameworks, preventing their shrinkage or collapse. Therefore, the presence of channels and pores facilitates rapid electrolyte diffusion, leading to an augmentation in electrical conductivity as shown by our results.

Fig 9 shows the difference of the current for each molecule X as a function of the voltage as:

$$S = 100\% \frac{|I_X - I_g|}{I_X}, \quad (5)$$

with I_X of each molecule and the surface and I_g the current of the graphene in a) and GPNL in b). Noticing that the adsorption of CH_x compounds increases the sensitivity of the surfaces. The tunneling currents for the sheets as a function of the voltage for various adsorbed molecules are shown in the inset plots by I-U characteristics graphs for voltages below 300 mV. Our results are in a qualitative good agreement with reported experimental data⁶ showing a decrease of 25 mV for GPNL and an efficiency increase of 4% for methane single molecules. Thus, the porous structure of GPNL offers distinct advantages, including increased surface area, reduced density, and improved accessibility to guest objects. This structure is highly suitable for applications involving light absorption and electron/ion transport. Specifically, it shortens the migration path of charge carriers from the point of generation to the active surface, thereby facilitating electron migration to the surface. Therefore, we suggest that GPNL based materials can be better candidates than graphene ones for use in field effect transistors, as Zener diodes, and faster sensors.

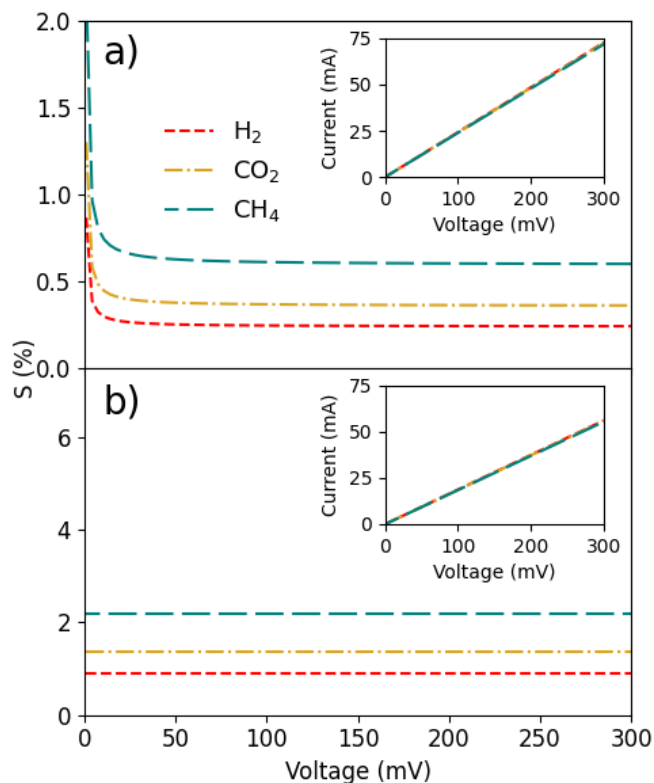


FIG. 9. Sensitivity of graphene in a) and graphenelyne in b) considering different molecules and atoms adsorbed. The inset shows the linear current-voltage (I-V) characteristics in the range of 0–300 mV.

IV. CONCLUSION

In this study, we utilize computer simulations to explore the gas separation mechanism and its impact on

the optical and electronic properties of graphene and graphenelyne sheets. Our focus is specifically on the emission behavior of CH_4 and CO_2 molecules. To conduct these simulations, we employ a quantum-classical molecular dynamics approach, utilizing the SCC-DFTB method with van der Waals corrections. These corrections are essential to accurately capture the dissociation, chemisorption, and molecule formation processes involved in the dynamics.

We analyze the probabilities of transmission, reflection, and adsorption of the emitted molecules. Our results highlight that GPNL exhibits significant advantages in gas separation compared to graphene. Specifically, we find that GPNL enables efficient separation of CO_2 into $CO+O$ and CH_4 into CH_2+H_2 with the highest probabilities to be dissociated. The porosity of GPNL enhances gas separation rates, facilitates CO_2 purification, and promotes hydrogen production from methane. By conducting electron transport calculations with the non-equilibrium green function method, we noticed that hydrocarbon like CH_2 , and CH_4 have the most effects on the electron transport mechanisms for both 2D materials.

ACKNOWLEDGEMENTS

We acknowledge support from the European Union Horizon 2020 research and innovation program under grant agreement no. 857470, from the European Regional Development Fund via the Foundation for Polish Science International Research Agenda PLUS program grant No. MAB PLUS/ 2018/8. We acknowledge the computational resources provided by the High Performance Cluster at the National Centre for Nuclear Research and the Interdisciplinary Centre for Mathematical and Computational Modelling (ICM) University of Warsaw under computational allocation no g91-1427.

¹ Jana R, Hajra S, Rajaitha P M, Mistewicz K and Kim H J 2022 *Journal of Environmental Chemical Engineering* **10** 108543 ISSN 2213-3437 URL <https://www.sciencedirect.com/science/article/pii/S2213343722014166>

² Balandin A A 2011 *Nature materials* **10** 569–581

³ Wang B, Gu Y, Chen L, Ji L, Zhu H and Sun Q 2022 *Nanotechnology* **33** 252001

⁴ Leenaerts O, Partoens B and Peeters F M 2008 *Phys. Rev. B* **77**(12) 125416 URL <https://link.aps.org/doi/10.1103/PhysRevB.77.125416>

⁵ You Y, Deng J, Tan X, Gorjizadeh N, Yoshimura M, Smith S C, Sahajwalla V and Joshi R K 2017 *Phys. Chem. Chem. Phys.* **19**(8) 6051–6056

⁶ Shaban M, Ali S and Rabia M 2019 *Journal of Materials Research and Technology* **8** 4510–4520 ISSN 2238-7854 URL <https://www.sciencedirect.com/science/article/pii/S223878541831370X>

⁷ Aligayev A, Raziq F, Jabbarli U, Rzayev N and Qiao L 2022 Chapter 17 - morphology and topography of nanotubes *Graphene, Nanotubes and Quantum Dots-Based Nanotechnology* Woodhead Publishing Series in Electronic and Optical Materials ed Al-Douri Y (Woodhead Publishing) pp 355–420 ISBN 978-0-323-85457-3 URL <https://www.sciencedirect.com/science/article/pii/B9780323854573000190>

⁸ Shanmugam V K, Mensah R A, Babu K, Gawusu S, Chanda A, Tu Y, Neisiany R E, Försth M, Sas G and Das O 2022 *Part. Part. Syst. Charact.* **39** 2200031

⁹ Gao F, Menchón R, Garcia-Lekue A *et al.* 2023 *Communications Physics* **6** 115

¹⁰ Hirsch A 2010 *Nature materials* **9** 868–871

¹¹ Karfunkel H R and Dressler T 1992 *Journal of the American Chemical Society* **114** 2285–2288

¹² Baughman R, Eckhardt H and Kertesz M 1987 *The Journal of chemical physics* **87** 6687–6699

- ¹³ Li Q, Ma Y, Oganov A R, Wang H, Wang H, Xu Y, Cui T, Mao H K and Zou G 2009 *Physical review letters* **102** 175506
- ¹⁴ Sheng X L, Yan Q B, Ye F, Zheng Q R and Su G 2011 *Physical review letters* **106** 155703
- ¹⁵ Lee G, Yang G, Cho A, Han J W and Kim J 2016 *Phys. Chem. Chem. Phys.* **18**(21) 14198–14204
- ¹⁶ Balaban A, Rentia C C and Ciupitu E 1968 *Revue Roumaine de Chimie* **13** 231–+
- ¹⁷ Balaban A, Klein D and Folden C 1994 *Chemical Physics Letters* **217** 266–270
- ¹⁸ Song Q, Wang B, Deng K, Feng X, Wagner M, Gale J D, MÅLllen K and Zhi L 2013 *J. Mater. Chem. C* **1**(1) 38–41
- ¹⁹ Villegas-Lelovsky L and Paupitz R 2020 *Phys. Chem. Chem. Phys.* **22**(48) 28365–28375 URL <http://dx.doi.org/10.1039/D0CP04188B>
- ²⁰ Du Q, Tang P, Huang H *et al.* 2017 *Scientific Reports* **7** 40796
- ²¹ Zhang R and Jiang J 2019 *Frontiers in Physics* **14** 13401
- ²² Brunetto G, Autreto P, Machado L, Santos B, Dos Santos R P and Galvao D S 2012 *The Journal of Physical Chemistry C* **116** 12810–12813
- ²³ Kochaev A, Meftakhutdinov R, Sibatov R and Timkaeva D 2021 *Computational Materials Science* **186** 109999 ISSN 0927-0256 URL <https://www.sciencedirect.com/science/article/pii/S0927025620304900>
- ²⁴ Martins N F, Fabris G S L, Albuquerque A R, Paupitz R and Sambrano J R 2022 *Graphenylene-Like Structures as a New Class of Multifunctional Materials Alternatives to Graphene* (Cham: Springer International Publishing) pp 209–230
- ²⁵ Mahdizadeh S J and Goharshadi E K 2020 *RSC Adv.* **10**(41) 24255–24264
- ²⁶ Xu J, Zhou S, Sang P, Li J and Zhao L 2017 *Journal of Materials Science* **52** 10285–10293
- ²⁷ Zhu L, Jin Y, Xue Q, Li X, Zheng H, Wu T and Ling C 2016 *Journal of Materials Chemistry A* **4** 15015–15021
- ²⁸ Rezaee P and Naeij H R 2020 *Carbon* **157** 779–787
- ²⁹ Motallebipour M S and Karimi-Sabet J 2021 *Physical Chemistry Chemical Physics* **23** 14706–14715
- ³⁰ Sangwan V K and Hersam M C 2018 *Annual Review of Physical Chemistry* **69** 299–325
- ³¹ Zhang J, Liu L, Yang Y, Huang Q, Li D and Zeng D 2021 *Phys. Chem. Chem. Phys.* **23**(29) 15420–15439
- ³² Chung W T, Mekhemer I M, Mohamed M G, Elewa A M, EL-Mahdy A F, Chou H H, Kuo S W and Wu K C W 2023 *Coordination Chemistry Reviews* **483** 215066 ISSN 0010-8545 URL <https://www.sciencedirect.com/science/article/pii/S0010854523000553>
- ³³ Wang Z, Zhou X F, Zhang X, Zhu Q, Dong H, Zhao M and Oganov A R 2015 *Nano Letters* **15** 6182–6186
- ³⁴ Whitener Keith E J 2018 *Journal of Vacuum Science & Technology A* **36** 05G401
- ³⁵ Hourahine B, Aradi B, Blum V, Bonafe F *et al.* 2020 *The Journal of Chemical Physics* **152** 124101
- ³⁶ Cui Q, Elstner M, Kaxiras E, Frauenheim T and Karplus M 2001 *The Journal of Physical Chemistry B* **105** 569–585
- ³⁷ Santos E and Schmickler W 2021 *Journal of Physics: Condensed Matter* **33** 504001 URL <https://dx.doi.org/10.1088/1361-648X/ac28c0>
- ³⁸ Arunragasa S, Seekaew Y, Pon-On W and Wongchoosuk C 2020 *Diamond and Related Materials* **105** 107790 ISSN 0925-9635 URL <https://www.sciencedirect.com/science/article/pii/S0925963520300674>
- ³⁹ Fabris G, Marana N, Longo E and Sambrano J 2018 *Journal of Solid State Chemistry* **258** 247–255
- ⁴⁰ Martins N F, Fabris G S, Albuquerque A R and Sambrano J R 2021 *FlatChem* **30** 100286
- ⁴¹ Elstner M, Hobza P, Frauenheim T, Suhai S and Kaxiras E 2001 *The Journal of Chemical Physics* **114** 5149–5155
- ⁴² Dominguez-Gutierrez F J, Krstic P S, Irle S and Cabrera-Trujillo R 2018 *Carbon* **134** 189–198
- ⁴³ Novotny M, Dominguez-Gutierrez F J and Krstic P 2017 *J. Mater. Chem. C* **5**(22) 5426–5433
- ⁴⁴ Dominguez-Gutierrez F J, Aligayev A, Huo W, Chourashiya M, Xu Q and Papanikolaou S *physica status solidi (b)* **n/a** 2200567
- ⁴⁵ Marquez D M and SÃ~nchez C G 2018 *Phys. Chem. Chem. Phys.* **20**(41) 26280–26287
- ⁴⁶ Oviedo M B, Negre C F A and SÃ~nchez C G 2010 *Phys. Chem. Chem. Phys.* **12**(25) 6706–6711
- ⁴⁷ Pecchia A, Penazzi G, Salvucci L and Carlo A D 2008 *New Journal of Physics* **10** 065022 URL <https://dx.doi.org/10.1088/1367-2630/10/6/065022>
- ⁴⁸ Lee G, Hong I, Ahn J, Shin H, Benali A and Kwon Y 2022 *The Journal of Chemical Physics* **157** 144703
- ⁴⁹ Lee C, Leconte N, Kim J, Cho D, Lyo I W and Choi E 2016 *Carbon* **103** 109–114 ISSN 0008-6223 URL <https://www.sciencedirect.com/science/article/pii/S000862231630197X>
- ⁵⁰ Zhang W, Lu W C, Zhang H X, Ho K and Wang C 2018 *Carbon* **131** 137–141 ISSN 0008-6223 URL <https://www.sciencedirect.com/science/article/pii/S0008622318301052>
- ⁵¹ Gui Y, Peng X, Liu K and Ding Z 2020 *Physica E: Low-dimensional Systems and Nanostructures* **119** 113959 ISSN 1386-9477 URL <https://www.sciencedirect.com/science/article/pii/S1386947719313116>
- ⁵² Hashemi M, Farzad M H, Mortensen N A and Xiao S 2013 *Journal of Optics* **15** 055003 URL <https://dx.doi.org/10.1088/2040-8978/15/5/055003>
- ⁵³ Kumar M R, Singh S, Fahmy H M, Jaiswal N K, Akin S, Shalan A E, Lanceros-Mendez S and Salado M 2023 *Journal of Power Sources* **556** 232256 ISSN 0378-7753 URL <https://www.sciencedirect.com/science/article/pii/S0378775322012332>